Can structure data obtained from CT images substitute for parameters of a preferential flow model?

A.-S. Lissy, S. Sammartino, S. Ruy

Can structure data obtained from CT images substitute for parameters of a preferential flow model?

Authors: Lissy A.-S.[(1)(2)], Sammartino S. [*(1)(2)], Ruy S. [(2)]

[(1)] Avignon Université, UMR EMMAH "Environnement Méditerranéen et Modélisation des Agro-Hydrosystèmes", F-84914 Avignon Cedex 09, France.
[(2)] INRAE, UMR EMMAH "Environnement Méditerranéen et Modélisation des Agro-Hydrosystèmes", F-84914 Avignon Cedex 09, France.

* Corresponding author: stephane.sammartino@univ-avignon.fr

Keywords: water flow modeling, Kinematic Wave Dispersion (KDW) model, Richards equation, 3D images, X-ray tomography, sensitivity analysis.

Highlights:

- Classical and advanced versions of a water flow dual-porosity model are presented
- Structure parameters from X-ray images are integrated in the advanced version
- Classical version gives best results but water exchange is not properly simulated
- Advanced version produces worse results but a new knowledge has been introduced
- Drainage dynamics (initial state: dried at a matric potential of -3.5 m) is controlled by water exchange among porosity domains

Abstract

Modeling preferential flow in soils is still a challenge for the scientific community working on water resources. Indeed, it is an issue to determine the functional parameters of models dedicated to water flow, that are currently obtained by fitting processes, whereas their relationships with soil structure remain poorly known. Improved models are expected from a better understanding of the links between functional and structural parameters, which can be achieved thanks to recent developments in imaging methods such as X-ray Computed Tomography (CT). The paper seeks to improve a dual-porosity model, coupling matrix flow (by Richards equation) and preferential flow (by a Kinematic Dispersive Wave), by substituting some model parameters, usually obtained by inversion of experimental data, by those assessed from CT images of the soil structure. Thus, two versions of the model are compared, the "classical" and the "advanced" one including parameters determined using the 3D images of the sample structures. To compare model versions with real situations, infiltration experiments were conducted in lab on two different soils at two initial water contents. An X-ray medical scanner allowing acquisitions of large soil volumes (≈ 1700 cm^3) with a voxel size of 400 µm was used to image the sample structures. Then, we derived two geometrical parameters from the macroporosity network: the percolating macroporosity and a characteristic dimension of this macropore network, the mean inter-macropore distance. The sensitivity analysis conducted on the classical version of the model showed that the kinematic coefficient and the dimensional parameter of the porous medium are the two main contributors to the cumulated drainage whatever the initial condition. Although experimental data are better simulated by the classical version of the model, drainage dynamics is also well simulated by the advanced version. However, differences between the model versions that are small for both soils at field capacity become significant for the dried state (mean initial matric potential of -3.5 m). This emphasizes the crucial effect of the sink-source term and in particular the complex effect of the dimensional parameter that it contains. Indeed, difficulties to simulate properly water exchange between porosity domains are encountered for both versions of the model. We conclude that empirical parameters that were up to now fitted from experiments could be deduced from geometrical indicators computed from CT images and that owning to these first results the applied methodology is promising to achieve a better understanding and modeling of preferential flow processes and to improve model predictability.

1. Introduction

Preferential flow in soil concerns all the phenomena by which water and solutes move along certain pathways, while bypassing a large fraction of the porous matrix (Hendrickx and Flury, 2001). Three preferential flow phenomena can be distinguished: finger flow, funnel flow and flow in macropores. While finger flow results from hydrodynamic instabilities at the infiltration front, when crossing soil discontinuities at a mesoscale, macropore flow is associated with porosity heterogeneity at a larger scale such as large interconnected pores (i.e. macropores) distributed within the soil matrix (Germann et al., 2007). Funnel flow can be induced by must larger macroscale heterogeneities (Nimmo, 2012 ; Jarvis et al., 2016)). Macropore flow occurs in a reduced part of the soil macroporosity , i.e. the accessible, more open, and interconnected fraction. This fraction is also called active, functional, percolating or connected macroporosity. Efforts to characterize and dynamically identify this fraction of the pore space have recently been reported (Jarvis et al., 2016; Katuwal et al., 2015; Mossadeghi-Björklund et al., 2016; Sammartino et al., 2015), most of them using the possibilities such as those offered by X-ray tomography to non-destructively image and characterize the internal soil structure. Although relatively little is known about the hydrodynamic processes and associated physicochemical mechanisms at the macropore surface, the effects of macropore flow in soils have been widely studied (Beven and Germann, 2013, 1982). Macropore flow can affect the partitioning between runoff and drainage, the response of the water table to rainfall events, and the groundwater quality as the filtering capability of the soil is not activated for macropore flow (Clothier et al., 2008). To account for preferential flow at soil profile scale, several water-flow models have been developed in the past three decades (Gerke, 2006).

The first models focused on preferential flow processes without accounting for matrix flow. In the macroporous domain, the gravitational movement of water is described by a Kinematic Wave equation (Beven and Germann, 1982; Gerke, 2006). Chen and Wagenet (1992) and Germann (1990) derived a functional relation between the mean water flux and the water content, with a Newton's law on shear and with a channel flow approach and combined this relation with the continuity equation. Thus, they developed the kinematic wave model (KW) for the modeling of fast water flow in macropores (Germann, 1985). Numerous results showed that the KW model was able to accurately simulate infiltration-drainage experiments when preferential flow process is dominant (Di Pietro and Lafolie, 1991; Germann and Di Pietro, 1996). However, results presented by (Germann et al., 1997) showed that the KW model overestimates macropore flow because friction and gravity forces are not balanced

immediately in transient flow regime and enhance dispersion of the wetting and draining front. Dispersion of water flow can be induced by the sum of capillary forces, spatial convective inertia effects and resistance forces due to complex pore paths (Di Pietro, 1998). Thus later, (Di Pietro et al., 2003) developed the Kinematic Dispersive Wave (KDW) model as a correction of the KW equation, to take into account fluid dispersion effects due to the local inertia forces that are dominant in large macropores. In the KDW model, it is assumed that the water flux is a nonlinear function of the mobile water content and of its first time derivative. In (Di Pietro et al., 2003), the KDW model was validated by comparison to experimental data. However, it was not coupled to a model, such as the commonly used Darcy-Richards equation for the modeling of slow water flow in the matrix, as is required in complex soils where slow matrix flow and rapid macropore flow can occur simultaneously and promote water exchange between the porosity domains.

Then models based on a dual porosity approach were developed, where each porosity domain has its own hydraulic properties and solute concentrations (Gerke and van Genuchten, 1993; Gwo et al., 1995; Jarvis and Boesten, 1998). These models account for macropore and matric flows, water and mass exchanges between the two domains. The main difference among existing dual-porosity models consists in the approach used to represent macropore flow as the exchange terms are conceptually quite similar, i.e. kinematic waves (Jarvis, 1994), or the Darcy-Richards equation with a high hydraulic conductivity (Gerke and van Genuchten, 1993). Most dual-porosity models have an exchange term between porosity domains which integrates some structural parameters. As far as we know, these parameters account for a mean macropore shape and the spatial arrangement of macropores. However they are not experimentally determined in an independent way, but are usually mathematically calculated with an inversion procedure applied to calibration data (Gerke, 2012). Consequently, most of the time, these parameters serve to adjust the model and their relationships with the structural properties of samples are far from being correctly understood.

The modeling approach that was used in the paper is a model developed by coupling two older models, the KDW model for macropore flow and the Darcy-Richards equation for matric flow. The coupling and modeling works were done using the interactive French modeling platform named Virtual Soil (https://www6.inra.fr/vsoil). The paper is dedicated to the comparison of two versions of this model: one named “classical” in which all parameters are inverted from calibration data, and one named “advanced” in which two parameters selected among the previous ones are independently assessed from the CT images of soil samples. The study was conducted following three steps. Firstly, a sensitivity analysis was

126 realized for a better understanding of the parameter sensitivity of the classical version of the
127 model. Secondly, this version was used to simulate the infiltration-drainage experiments
128 performed on the undisturbed soil columns under simulated rainfalls and for contrasted initial
129 soil moistures (the field capacity and the dried state at -3.5 m of matric potential). Parameters
130 of the classical model version were adjusted on calibration data for each soil and experiment.
131 Thirdly, the additional knowledge provided by the CT images of sample structures was
132 introduced in our model to create the advanced version. Two structure features of the soils
133 were derived: the volume of the percolating =macroporosity and a dimension of this percolant
134 network, which was chosen to characterize the spatial distribution of macropores over the
135 sample height: the mean inter-macropore distance. These parameters were then integrated in
136 the advanced version of the model. The quality of the cumulative drainage and storage
137 simulated during infiltration experiments and the distribution of water flow in the porosity
138 compartments are finally discussed.

139 **2. Materials and Methods**

140 *2.1 Soil sampling and soil characteristics*

141 Two undisturbed soil cores of two different soils with contrasted textures and structures were
142 sampled for the infiltration experiments (Table 1). The first one is a Loamy soil (Calcisol
143 Chromic Cambisol, WRB) with a grainy structure (43.948790, 4.461378). The second one is a
144 Silty soil (Calcaric Fluvisol, WRB) with polyhedral aggregates due to shrinkage and swelling
145 of clay minerals and showing numerous tubular macropores due to earthworm activities
146 (43.915343, 4.882514).

147 Two additional samples were collected for each soil to determine the hydric properties of the
148 soil matrix with Wind's evaporation experimental setup (Wind, 1969). As the Wind sample is
149 7 cm in height (15 cm in diameter), hydrodynamic properties were determined on two soil
150 layers, each 7 cm in height. This total layer of 14 cm is strictly included in the first soil
151 horizon. The sampling of columns and Wind samples followed the protocol given by (Tamari
152 et al., 1993) to extract soil cores with minimal disruption. A soil column was obtained by
153 slowly inserting a PVC tube (12.5 cm inner diameter and 20 cm height), equipped with a
154 sharp cutting tool at its end, into the soil while step-by-step gently removing the soil around
155 the tube to minimize friction and shear forces. After sampling, a PVC grid with 1 mm
156 diameter holes drilled every 1.5 mm was stuck at the bottom of the column to restrain the loss
157 of soil aggregates during water drainage. The grid is not necessary for Wind samples and their
158 sample holder is a metal ring (7 cm height) drilled every 1 cm in height for the lateral

159 insertion of pressure probes. Columns and Wind samples were stored enclosed in a plastic bag
160 at 4 °C to avoid germination and earthworm displacement before the first experiment. A small
161 quantity of chloroform was poured on the upper surface of the column samples in order to
162 stop soil macrofauna activity and avoid soil structure evolution during storage and
163 experiments.
164 For each soil, one column was used for infiltration experiments and 3D X-ray image
165 acquisition of soil structures. The second one was equipped with 6 pressure probes for
166 monitoring the evolution of the matric potential in order to determine the distribution of the
167 initial water content over the sample height. The soil columns thus equipped were not scanned
168 but remained in the laboratory. It is important to mention that these twin columns (those for
169 infiltration experiments and those for the recording of matric potential) underwent the same
170 history since their sampling (same storage conditions, same infiltration experiments, same
171 delay between experiments). The sample drying was a slow drying at the controlled ambient
172 conditions of the air-conditioned lab (mean temperature of 22°C and mean air humidity
173 content of 45%). The infiltration experiments and the image acquisitions of soil structures
174 were thus conducted at two initial water contents, 1) the field capacity which means that soil
175 matrix should be saturated and the percolating macroporosity should have drained, and 2) a
176 drier water content intermediate between the field capacity and the wilting point of plants,
177 named “dried at h = -3.5 m”. The state is reached when the mean of the pressure probes of the
178 equipped columns indicate a matric potential near of -3.5 m. In the following text and
179 legends, the moisture status “dried at h = -3.5 m” can be indicated by “DS” as well as the field
180 capacity by “FC”.
181
182 *2.2 Soil hydrodynamic properties*
183 Wind samples are used for the determination of soil hydraulic properties (water retention and
184 hydraulic conductivity curves). Hydraulic conductivity of the saturated soil ($K_{sat\text{-}meas}$, $m.s^{-1}$)
185 was measured using a constant head permeameter (Dirksen, 1998). The $K_{sat\text{-}meas}$ of
186 undisturbed samples was measured including all porosities (micropores and macropores). Soil
187 matrix hydraulic properties were determined with the Wind evaporation method (Tamari et
188 al., 1993; Wind, 1969). Retention and hydraulic conductivity curves were fitted by the Wind
189 algorithm that uses the Mualem-van Genuchten model (Schaap and Leij, 2000; Van
190 Genuchten, 1980). The porosity (ε) was calculated using the relation between bulk density

191 (ρ_d) and soil particle density (ρ_s): ($\varepsilon = 1 - \frac{\rho_d}{\rho_s}$). All the hydrodynamic properties are
192 summarized in table 2.
193
194 *2.3 Device and infiltration experiments*
195 A specific device that was designed to be placed in a medical scanner was used (Fig.1). It
196 allows the recording of water fluxes together with discrete acquisitions of 3D images during a
197 rainfall event simulated inside the scanner. The device structure is made of wood without any
198 metal parts. The soil core is placed on the wooden table which is supported by two precision
199 scales (B1 and B2) to measure soil column weight during the infiltration-drainage experiment.
200 A third precision scale (B3) measures the water quantity drained at the sample bottom. The
201 three scales are connected to a computer and recorded continuously during the experiment
202 from the beginning of rainfall to the drainage after the rainfall is stopped. No scales or metal
203 parts are included in the field of view of the scanner to avoid scanning artifacts. The rainfall
204 simulator is composed of a plastic tank with hypodermic needles arranged on a squared mesh
205 on the bottom surface (0.4 mm inner diameter every 1.5 mm). It is connected to a pulse pump
206 whose piston volume and pulse frequency are adjusted to control the simulated rainfall
207 intensity.
208 Three preliminary infiltration experiments were performed in the laboratory to gradually
209 saturate the soil in order to reach the field capacity. This water content is a conceptual vision
210 of the water distribution in which the soil matrix is assumed to be fully saturated with
211 macropores completely drained. During these first experiments, water fluxes and column
212 weight were also measured to control the mean water content. Following these preliminary
213 tests, two rainfalls were made inside the medical scanner, the first one at field capacity and
214 the second one far from the field capacity (dried to a water potential of 3.5 m). For each
215 rainfall event, the rainfall simulator was set to deliver intensity near of 20 $mm.h^{-1}$ for duration
216 of one hour and a half. These values were chosen to simulate a thunderstorm that usually
217 occurs several times per year in the French Mediterranean region. Each simulated rainfall
218 event delivered 30 mm of water to the soil. The weight of the soil column was recorded every
219 10 s from the beginning of the rainfall to half an hour after stopping the rainfall (120 min.).
220 Throughout the duration of the experiment, several 3D images were acquired to monitor water
221 infiltration within the soil core but for this study we used only the first image acquired before
222 the rainfall event began, taken as the reference for the initial soil structure and water content.
223 At field capacity, the rainfall intensity was 20.2 $mm.h^{-1}$ and the initial mean matric potential

was around -0.05 m for the Loamy soil (resp. 20.5 mm.h^{-1} and -0.15 m for the Silty soil). In the initial wet state, the rainfall intensity was 23.5 mm.h^{-1} for the Loamy soil (resp. 21.7 mm.h^{-1} for the Silty soil) and the initial mean matric potential was around -3.5 m for the two soil samples.

2.4 The flow model accounting for preferential flow

The model simulates slow water flow driven by capillarity and gravity in the soil matrix with the Richards equation and fast gravity-driven flow in the macroporosity with the Kinematic Dispersive Wave equation (Di Pietro et al., 2003). Water flow between the two soil porosity domains is calculated by a sink-source term.

2.4.1 Richards equation

The Richards equation for the soil matrix is:

$$\frac{\partial \theta_{mi}(h)}{\partial t} + \frac{\partial}{\partial z}\left(-K_{mi}(h)\frac{\partial (h-z)}{\partial z}\right) = S \; ; \qquad \text{[Eq. 1]}$$

where: θ_{mi} (m^3.m^{-3}) is the water content of the soil matrix; h (m) is the matric potential; K_{mi} (m.s^{-1}) is the hydraulic conductivity of the soil matrix, S (m^3.m^{-3}.s^{-1}) is the sink-source exchange term and is described in the following section.

2.4.2 Kinematic Dispersive Wave and sink – source term

As stated by Di Pietro et al. (2003), when non conservative forces that induce attenuation of the kinematic water wave are present, the macroscopic water flux q_{ma} depends on the mobile water content θ_{ma} and also on its derivatives. In Di Pietro et al. (2003), a time derivative of θ_{ma} was chosen to account for these inertial forces. In this paper the time derivative is replaced by a space derivative for improving the numerical resolution and reducing numerical defaults. The $q_{ma}(\theta_{ma})$ relationship is now written as:

$$q_{ma} = b\theta_{ma}^{a} - \nu_\theta \frac{\partial \theta_{ma}}{\partial z} \qquad \text{[Eq. 2a]}$$

where: b (m.s^{-1}) is the kinematic coefficient, a (–) is an empirical parameter qualitatively related to the shape of the macropores and the laminar/turbulent nature of water flow in macropores (Ruy et al., 1999). ν_θ (m^2.s^{-1}) is similar to a diffusion coefficient and account for the importance of inertial effect and capillary diffusion compared to the pure convective effect of the KDW model (Di Pietro et al., 2003). Introducing this relationship in the water balance

equation of the macropore network and taking into account the exchange term with the matrix domain leads to the following equation:

$$\frac{\partial \theta_{ma}}{\partial t} + c\,\frac{\partial \theta_{ma}}{\partial z} - \nu_\theta \frac{\partial^2 \theta_{ma}}{\partial z^2} = -S \qquad \text{[Eq. 2b]}$$

where θ_{ma} is the water content in macropores; $c = \left.\frac{\partial q_{ma}}{\partial \theta_{ma}}\right]_{\frac{\partial q_{ma}}{\partial z}=cte} = ab\theta_{ma}^{a-1}$ (m s^{-1}) is the velocity of the infiltration front.

The Richards and the KDW equations are coupled with the exchange term *S* (Eq. 3) which is slightly modified from (Ruy et al., 1999) by assuming that the water potential in the macropore network is equal to 0:

$$S = -\frac{K_{mi}(h)}{d} \times \frac{-h}{d} \times \frac{\theta_{ma}}{\theta_{max-mac}}\,; \qquad \text{[Eq. 3]}$$

where: d (m) is a shape parameter of the macroporosity, a characteristic size of the porous media, called inter–macropore distance in the rest of this article; $\theta_{max-mac}$ ($m^3.m^{-3}$) is the saturated water content in the macroporosity.

2.4.3 Estimation of KDW and sink – source term parameters

Two versions of the model were studied and compared. The first version, named "classical", corresponds to the modeling where the unknown parameters of the model are fitted from rainfall-drainage experiments by an inverse modeling method. The second version, named "advanced", corresponds to an innovative modeling where the unknown structural parameters used in the sink term are computed from an advanced processing of 3D images of the soil structure.

- ***Classical version of the model***

KDW (a, b, ν_θ) and sink – source term (d and $\theta_{max-mac}$) parameters were estimated using the DREAM algorithm for each of the four experiments. This method is a global optimization algorithm that provides an exact Bayesian estimate of uncertainty (for more details see (Vrugt, 2016; Vrugt et al., 2008).

The variation range of each parameter is presented in Table 3. However, as *a* and *b* are correlated (Ruy et al., 1999), we could not use the DREAM algorithm directly. To deal with this correlation, we assumed that the hydraulic conductivity of the measured saturated soil matrix can be neglected compared to the water flow in the macropore network. This assumption is based on the measured value of $K_{sat\text{-}meas}$ obtained on undisturbed soil cores with large macropores that is more than two orders of magnitude higher than the calculated value

of K_{mi} obtained with the Wind's method at matrix near saturation. Thus, we obtain the following relationship for the flow at steady state under a unit gradient and full saturation of the soil core:

$$K_{sat-meas} \approx b \cdot \theta_{max-mac}^{a} \quad \text{[Eq. 4]}$$

where $K_{sat-meas}$ is the hydraulic conductivity measured previously in the laboratory, and $b \cdot \theta_{max-mac}^{-a}$ is the water flux through the macroporosity. Eq. 4 shows that for a given soil, parameters b and a are not independent. In the first step, the value of a was successively set to $1, 2, 3, 4, 5, 6$. For each value of a, a theoretical value of b was computed from Eq. 4 by using the median value of measured macroporosity profile $\theta_{\max-mac-meas}$:

$$b_{th} = K_{sat-meas} \times \theta_{max-mac-meas}^{-a} \quad \text{[Eq. 5]}$$

This value was used to set the variation range in which the DREAM algorithm searches the value of b for fitting, see Table 3. For each value of a, DREAM fits the set of parameters (b, d, v_θ and $\theta_{max-mac}$) by minimizing the error between observation and simulation curves. We then defined a restricted search interval for a according to the lower temporal error. This restricted interval is used in the second step whose purpose is the estimation of all parameters (a, b, d, v_θ and $\theta_{max-mac}$) using the DREAM algorithm on restricted intervals for a (search intervals [a_{min} ; a_{max}]) and b search interval as :

$$\left[\frac{(K_{sat-meas} \times \theta_{max-mac-meas}^{-a_{max}})}{5}; (K_{sat-meas} \times \theta_{max-mac-meas}^{-a_{min}}) \times 5\right] \quad \text{[Eq. 6]}$$

Search intervals for other parameters are reported in Table 3. Experiments were simulated with these parameter sets, and the final fitting was evaluated using the temporal error curve.

- ***<u>Advanced version of the model incorporating additional knowledge provided by the 3D imaging.</u>***

The assumption behind the advanced version of the model was that some parameters, which are usually estimated by inversion, could be replaced with the data obtained independently thanks to the 3D images of the sample structure. In this advanced version, KDW parameters (a, b and v_θ) are estimated by the DREAM method as was the case in the classical version, but two parameters (d and $\theta_{max-mac}$) controlling the sink-source are obtained thanks to image data. Moreover, we replace a unique value of two sink-source term parameters by a profile of around 400 values measured over the height of the soil column which permits accounting for soil structural heterogeneity and the unidirectional nature of the model on the Z-axis. The fitting methodology of KDW parameters is the same as previously.

319 *2.4.4 Sensitivity analysis*

320 The sensitivity analysis was performed to increase our model understanding in the transient
321 and pseudo-stationary regimes and to quantify the importance of each parameter and their
322 interaction effects. The study was conducted in particular to highlight the effect of initial
323 water content on parameter sensitivity using the classical version of the model.

324 The sensitivity analysis (SA) was performed on one model output recorded during
325 experiments: the cumulative water drainage. The SA was conducted on parameters of the
326 KDW model and of the sink-source exchange term using the FAST 99 method based on the
327 Fourier Amplitude Sensitivity Test. This method estimates the contribution of each input
328 factor to the output's variance (Saltelli et al., 1999); the chosen variation ranges are the same
329 as those for the first step of the DREAM estimation (Table 3). FAST calculates two indexes
330 for each parameter: (1) the principal contribution, and (2) the total contribution, to the
331 variance of the output variable. For a given parameter, the difference between the two indexes
332 represents the interaction effects of this parameter with the other parameters: it is the part of
333 the output variable variance explainable by interactions between all tested parameters.

334

335 *2.5 X-ray scanner, acquisition and image processing methods*

336 Helical acquisition is designed to strongly diminish the acquisition time of medical scanners.
337 This device was therefore chosen to acquire the reference image taken before the rainfall was
338 started and the series of time-resolved images that were not used in this study. The images
339 were acquired with a Siemens SOMATOM Definition AS 128 slices CT scanner, equipped
340 with multi-detector rows that can acquire 128 slices simultaneously. It is located in the "Val
341 de Loire" center of the French National Institute for Agricultural Research and Environment
342 (INRAE); for more details see (Sammartino et al., 2015). The system setting to optimize
343 acquisition is an acceleration voltage of 140 kV, a tube current of 400 mA, and a pitch factor
344 of 0.35. The table feed is 12.35 $mm.s^{-1}$. The entire soil volume is thus scanned in 10 s.

345

346 *2.5.1. Pre-processing and macroporosity thresholding*

347 Tomographic sections were reconstructed using the Siemens software that applies a filter to
348 enhance object edges and remove beam hardening. No more additional information can be
349 obtained on the reconstruction step. In medical tomography, the image grey levels are
350 calibrated to the Hounsfield scale which transforms attenuation coefficients into local bulk
351 densities, based on the X-ray attenuation by water and air. Tomographic images are given in

the 12-bit signed DICOM format (Raw CT data). Pre-processing and processing of image series were applied by following the methodology given in Sammartino et al. (2012). At the end, the sample holder is removed from the region of interest, images are cropped and resliced in order to obtain cubic voxels with a side of 400 µm, and a forbidden color is applied to the background. The macroporosity thresholding was also performed according to the procedure given in Sammartino et al. (2012) that uses a mixing law between air, infiltration water and soil matrix, and hypotheses on the voxel content to determine the thresholds to apply. Indeed, as these images are calibrated in "density" by the Hounsfield scale, a simplified attenuation model was developed and used. It is based on X-ray attenuation of water and soil matrix, and on the porosity and water saturation. Making hypothesis on the distribution of water, air and soil matrix in one voxel, values of the thresholds in the Hounsfield scale can be calculated using the simplified model (Sammartino et al. 2015). Owing to the voxel size, all the voxels fulfilled with air or water were classified in the macroporosity compartment. By following this approach having in mind an image analysis point of view, all the voxels fulfilled with more than half air or water were also classified in macroporosity. The other voxels were put in the soil matrix compartment. The applied thresholds in the Hounsfield scale were respectively for the field capacity and the dried state at -3.5 m, 468 and 478 for the loamy soil, and 498 and 510 for the Silty soil. After thresholding, the quality of segmentation was checked on several slices randomly chosen in the stacks by superimposing outlines of the macroporosity phase on grey level images in a transparent-paste mode. Then, the raw CT data were transformed into binary images from which morphological and topological parameters associated with the macropore networks can be quantified. All the pre-processing was performed with ad-hoc macros and plugins developed and used with the public domain software ImageJ (Schneider et al., 2012).

2.5.2. Determination of new parameters for the dual-porosity model

We focused on the percolating =macroporosity as described by Sammartino et al. (2015), i.e. the interconnected pathways within which fast flow can occur under gravity. These authors showed by adding brilliant-blue to a water infiltration experiment that the active part of the porosity was quite similar to the percolating part of the macroporosity, i.e. the macropore network that connects the input and output surfaces of the soil column. To derive this percolating network from the whole macroporosity, the tool “Axis connectivity” of Avizo® was applied in the column height direction. This tool is usually used to segment the part of porosity that is connected to the input and output surfaces of a sample in a given direction. In

three-dimension, the structuring element was a 26-voxels neighborhood and the propagation axis, the Z-axis (sample height). Macropores are labellized and then we retain the most important one that connects both sample sections.

The sink-source term defined previously, which controls lateral flow from macropores to the soil matrix, depends on a characteristic size of the porous medium. This dimension is usually assimilated to a representative aggregate size by analogy to homogeneous porous media. In heterogeneous porous media, such as macroporous soils, it seemed necessary to account for the spatial distribution of structural heterogeneities in the definition of this characteristic size. We chose to determine the average half-distance between macropores of the percolating macroporosity using a Voronoï Diagram (named after the mean inter-macropore distance). This diagram gives a set of points that have an equal distance to the closest objects, i.e. the medial axis between objects. The average half-distance is obtained at each slice and objects are thus considered as macropore sections intercepted by each slice (Fig. 2e). The inter-macropore distance profile is calculated with an ad-hoc R script (Fig. 2g). Fig. 2 sums up the main processing steps applied to the 3D images. At the end, inter-macropore distances and percolating macroporosity profiles are obtained and discretized on approximately 400 values on sample height.

3. Results

3.1 Classical version of the model

3.1.1 Sensitivity analysis (SA)

Fig. 3 presents the temporal evolution of the principal index (dotted lines) and total contribution index (solid line) for each tested parameter of the KDW model and of the sink-source term. The SA was performed for the two studied soils at two initial moisture conditions for different values of a ranging from 1 to 6. However only one value of a per graph is presented as results obtained for other values do not significantly change the hierarchy of indexes and the conclusions drawn. The grey shaded area on each graph shows the variability of the cumulative drainages calculated over the 1200 runs of the SA. When the area reaches the x-axis, as shown in Fig. 3b and 3d, this means that breakthrough did not occur in at least one of the runs. Before the start of drainage (roughly between 500 and 1000 s), parameters b and ν_θ of the KDW model and parameter d of the sink-source term are the main contributors irrespective the soil and the initial soil moisture condition. The impacts

of these parameters on the cumulative drainage are mainly due to parameter interactions as the principal contribution index is far below the total contribution index.

The contribution of a given parameter to variations in cumulative drainage is a function of time after the drainage onset and this evolution may depend on the soil, on the initial soil moisture and also on the parameter itself. However, the impact of parameter ν_θ depends neither on the soil type nor on the initial soil condition: it always decreases with time and its principal order index is about 0. Therefore, this parameter has no or only very little direct impact on the overall cumulative drainage.

At field capacity initial condition, Loamy and Silty soils behave differently. Cumulative drainage of Loamy soil is mainly sensitive to parameter b and then to parameter $\theta_{max-mac}$, and the influence of the parameter $\theta_{max-mac}$ increases with time. Cumulative drainage of Silty soil is sensitive to b, d and $\theta_{max-mac}$ parameters. However, for Silty soil at the end of the simulation ($t = 7200\ s$), the principal contribution index of parameter d is about 0.5. This means that about 50 % of the variation of cumulative drainage at $t = 7200\ s$ is due to variations in the value of parameter d. For this soil, that has not been rehydrated enough by the three preliminary rains, the field capacity initial condition did not exactly correspond to the saturation of the soil matrix (matric potential around -0.15 m).

In the initial dried state (h = -3.5 m), the cumulative drainage is mainly sensitive to parameter d of the sink-source term and then to parameters b and $\theta_{max-mac}$, d and $\theta_{max-mac}$ have an impact on the quantity of water entering the soil matrix from the matrix-macropores interface. The greater d is, the lower the quantity of water entering the soil matrix is and the greater the cumulative drainage is.

3.1.2 Parameter adjustment by DREAM inversion

The cumulated drainage was used to adjust model parameters with the DREAM algorithm and water stored was taken as validation-verification data.

3.1.2.1 Calibration

Simulated and observed cumulated drainage curves are presented in Fig. 4 as well as the time evolution of error between observed and simulated curves. Data from the advanced version of the model will be discussed in part 3.2.

The graphs on the top line show a very close agreement between simulated and measured cumulative drainages. At the end of the experiment, the difference between the total amount of the simulated and measured drainage was less 1 mm (about 3 to 4% of the total amount of measured drainage). The central part of the graph, which represents the quasi-steady state of

451 the infiltration-drainage experiment, is very well simulated. According to the temporal error
452 evolution, estimations are noticeably better for experiments initially at field capacity than for
453 those initially at the state dried at h = -3.5 m. In detail, the first transition between flow
454 regimes can be highlighted by an increase in the error curve. Indeed, error values are always
455 small before breakthrough and increase during breakthrough, characterizing a less accurate
456 estimate of drainage during this transient state.
457 The main differences can be observed at the beginning of the experiment (drainage onset and
458 breakthrough time) and small differences can be observed at the end of the experiment (end of
459 pure drainage after the rainfall was stopped).

460 3.1.2.2 Verification on water storage

461 The total amount of water stored in the column during the infiltration experiment was used to
462 verify the model prediction after parameter calibration. As shown in Fig. 5 (top line), (i)
463 before water breakthrough, the amount of stored water increases linearly with the water
464 supplied by the rainfall simulator, (ii) after this transient state, a quasi-stationary flow regime
465 is reached. The slope of the plateau indicates whether water exchanges occur between
466 macropores and the soil matrix (non-zero slope) or not (zero slope).
467 The main discrepancies between simulations and measurements occur during the transient
468 state at the drainage onset: the amount of water stored in the soil column may be greatly
469 overestimated (resp. underestimated) for the Loamy soil (resp. Silty soil) in the field capacity
470 initial condition (resp. in the initial dried state at -3.5 m). However at the end of the
471 experiments, differences between the simulated and measured amount of water stored in the
472 soil column are small: they are always less than 1 mm (resp. 2 mm) for a measured water
473 amount of 3 mm (resp. between 6 to 11 mm) in the field capacity initial condition (resp. in the
474 initial dried state at -3.5 m). Moreover, it can be seen that the simulated curve is parallel to the
475 measured curve in the central part of each graph, whatever the initial soil water content. The
476 central part of each graph corresponds to the pseudo steady-state. This part can be almost flat
477 when the quantity of water entering the soil matrix from the macropore walls is negligible,
478 which is the case in the field capacity initial condition. The slope of this part can be positive
479 when water flow from macropores to the soil matrix is significant, which is the case for the
480 initial dried state at -3.5 m Considering that simulated and measured curves are parallel, this
481 means that water flow from macropores to the soil matrix is well simulated by the model.
482 Finally, at the end of the experiments, the discrepancy between simulated and experimental
483 data ranges between 0 and 0.5 mm for simulations conducted in the field capacity initial

condition and between 0.7 and 1.1 mm for simulations conducted in an initial dried state. All the parameters estimated are given in table 4.

3.2 Advanced version of the model

The sensitivity analysis showed that the characteristic dimension of the porous media (d) and the saturated water content in the macroporosity, i.e. the maximum accessible volume of macroporosity ($\theta_{max-mac}$) are two highly sensitive parameters of the model. We assumed that these parameters could be measured thanks to the 3D images of our undisturbed soil columns obtained from the X-ray scanner. They were thus assessed respectively by the inter–macropore distance and the percolating macroporosity.

3.2.1 CT image

3.2.1.1. Global properties

The mean inter-macropore distance, the percolating and entire macroporosities are presented in table 5 for both initial water contents. The 3D renderings of the macroporosities in figure 6 underscore the high complexity of the porous structures studied and consequently the challenge of giving a synthetic understandable representation. As a first understanding, samples seem to have macroporosities with variable extents and shapes. Some tubular macropores can be identified and associated to earthworm activity, whereas numerous isolated macropores can be associated with the aggregated structure. The percolating macroporosity is more extended in the Silty soil than in the Loamy one.

The average properties of entire and percolating macroporosities given in table 5 show that these macroporous structures are well above the percolation threshold, with 70 to 85 % of the macroporosity connected and percolating, respectively for Loamy and Silty soil.

At field capacity, the macroporosity of the Loamy soil is 23 % greater than that of the Silty soil, whereas it is almost equal when the initial matric potential is dropped to -3.5 m. For the Loamy soil (respect. Silty soil) containing 14% of clays (respect. 45% of swelling clays), the macroporosity increases of 3% (respect. 27%) from field capacity to the dried state at h = -3.5 m. The macroporosity variations from the field capacity to the dried state at h = -3.5 m, and between soils, depends on clay content and mainly result of an internal shrinkage of the soil matrix with negligible variations of the global sample height.

The behaviour of the percolating macroporosity is identical to those of entire macroporosity and whatever the soil when the initial moisture condition is changing from the field capacity to the wet state: the macroporosity increases and the mean inter-macropore distance decreases. However, this induces small variations for Loamy soil and more significant

variations for the Silty sample (Table 5). Indeed, macroporosity of the silty soil changes from 7.2 to 9.3 % (variation of 27 %) and those of the loamy soil, changes from 7.7 to 8.2 % (variation of 6 %). A same tendency can be seen for the mean inter-macropore distance.

The macroporosity of the Loamy sample, which is more diffuse (Fig.6), shows the smallest mean inter–macropore distance, slightly dependent on the initial moisture condition , in the order of 4 to 5 mm. This distance is multiplied by two when accounting for the percolating macroporosity. For the Silty sample, this increase is much smaller but more dependent on the initial moisture condition, as shown by the 7.8 mm value of the percolating macroporosity in the initial dried state at h = -3.5 m.

3.2.1.2 Profiles of macroporosity and inter-macropore distance properties

Visualizing and analyzing macroporosity variations on sample height is important because of the mono dimensional nature of the model oriented on the vertical axis, Z (Fig. 7). Z-profiles of Loamy soil macroporosity provide the crucial information that the overall shape of the profile does not evolve according to water content or when comparing entire and percolating macroporosity. These profiles are almost superimposable by translation. Their vertical shifts reflect the overall evolutions given in Table 5. The most significant deviations, although weak, are present in the lower part of the column between 0.10 and 0.14 m depth, for the profile of the percolating macroporosity in the case far from the field capacity (column a, light blue dotted line in Figure 7). The same remarks can be made for Silty soil on the shape profiles similarity, with however increasing discrepancies when moving from 0.05 m depth towards the column top. This is probably due to a preferential drying from the column top.

3.2.2 DREAM inversion

Results of the calibration and the validation steps for the advanced model version are presented respectively by green curves in Figures 4 and 5.

3.2.2.1 Calibration

Water drainage simulated by the advanced version of the model is close to the observed data and to simulations obtained with the classical version for soil cores at field capacity (Fig. 4). For the initial dried state at h = -3.5 m, small differences between simulation and measurements can be observed for the Silty soil: the simulated breakthrough time is considerably lower than the observed one and the slope of the simulated curve in the central part of the graph is lower than the experimental one. The result is a slight underestimation of

about 4 % of the overall water amount drained out of the soil core. These differences between simulation and measurement are larger for the Loamy soil in the initial dried state and the model underestimates the drained water amount by 18 %. These results are both due to an overestimation of the rewetting of the soil matrix by the advanced model version.

3.2.2.2 Validation – Verification

The water storage simulated by the advanced version of the model is close to observations and simulations made by the classical version for samples initially at field capacity. The gaps between simulated and measured data are also similar (Fig. 5). For the Silty soil at the initial dried state at -3.5 m, the global dynamic is close to the observation for the both models' versions but the rewetting phase of the soil matrix occurring between 500 to 5400 s is more poorly simulated by the advanced version of the model than by the classical one. For the Loamy soil in the initial dried state, the advanced version of the model fails to reproduce the water flow dynamic, contrary to the classical one.

4. Discussion

4.1 Sensitivity of model parameters

Sensitivity analysis (see Fig 3) applied to the classical version of the model showed that the kinematic coefficient (b), the inter–macropore distance (d) and to a lesser extent the maximum accessible macroporous volume ($\theta_{max-mac}$) are the main controlling parameters of the model outputs (drainage and water storage). By applying the sensitivity analysis in two realistic initial moisture conditions, we also outline that the model is sensitive to the initial water content.

At field capacity the kinematic coefficient (b) is the most sensitive parameter whereas the inter-macropores distance (d) is a sensitive parameter for Silty soil only. As there are no or few water exchanges between the two porosity domains, the model is less sensitive to the parameters involved in the sink–source term, such as d *or* $\theta_{max-mac}$. Moreover, the sensitivity analysis shows a high index of interaction between b and $\theta_{max-mac}$ parameters for Loamy soil and between b, $\theta_{max-mac}$ and d parameters for Silty soil: compensation effects between those parameters are likely to occur during the second part of the infiltration experiment.

The high sensitivity to parameter b was also underlined by Di Pietro et al. (2003) for the KDW model. Parameter b is related to the flow velocity in the macropore network: the model is very sensitive to this parameter when macropore flow is the dominant process of water flow

583 and when rewetting of the soil matrix from macropore walls is negligible, which is the case
584 for the field capacity initial condition. For Silty soil, we suppose that the field capacity initial
585 condition was not fully achieved so that a residual rewetting of the soil matrix was still
586 possible during the infiltration experiment.
587 At the dried state (h = -3.5 m), b and d parameters are the two sensitive parameters. The
588 compensation index is less important, so there is probably less interaction effect between
589 those parameters for the dried state than at field capacity. The breakthrough time constitutes a
590 limit between the dominance of the kinematic coefficient contribution (before breakthrough)
591 and the dominance of the inter–macropore distance (d) that increases and becomes important
592 after breakthrough.
593 The ν_θ parameter that controls kinematic wave attenuation has only a negligible influence on
594 the variance of cumulative drainage over time whatever the initial hydric situations, as already
595 noticed by Di Pietro et al. (2003). However, this parameter linked to the dispersive process of
596 the water flow is essential to reproduce the smooth transitions between the different flow
597 phases: beginning of the drainage after breakthrough, transition to the pseudo-steady-state and
598 beginning of the drainage recession after rainfall has stopped.
599 To conclude, as a rule of thumb, we can say that:
600 - (i) the parameter ν_θ of the KDW model has practically no or only very little impact
601 on the cumulative drainage, whatever the soil and the initial soil moisture condition;
602 - (ii) the parameter b of the KDW model is the main sensitive parameter of the
603 cumulative drainage for the field capacity initial condition;
604 - (iii) the parameter d is the most sensitive parameter to the cumulative drainage for the
605 initial dried state,
606 - (iv) parameters b, d and $\theta_{max-mac}$ show significant interactions, mainly at field
607 capacity initial condition It is important to find a way to independently measure
608 parameter d and $\theta_{max-mac}$ to avoid interactions and possible compensation effects
609 with parameter b.
610
611 *4.2 Parameters of the sink-source term*
612 In Table 4, fitted d and $\theta_{max-mac}$ parameters can be compared to the same parameters
613 obtained for X-ray CT images. Fitted value of $\theta_{max-mac}$ may be slightly different to the mean
614 value of the $\theta_{max-mac}(z)$ profile calculated from CT images: the difference may range
615 between 2% (Silty soil at h = -3.5 m) to 30% (Silty soil at field capacity). On the one hand,

$\theta_{max-mac}$ parameter is not a very sensitive parameter of classical model (see Fig. 3) and its sensitivity is due to interaction effects with others parameters (d and b) therefore the fitted value of $\theta_{max-mac}$ may be estimated with a large uncertainty. On the other hand, this parameter has a nonlinear impact on the overall water flow dynamic as the sink source term is inversely proportional to $\theta_{max-mac}$ (see eq. 3): the $\theta_{max-mac}(z)$ profile may therefore not be directly replaced by a single value.

We also observe that the fitted value of d is 3 et 10 times higher than the mean value of $d(z)$ profile calculated from CT images. Three hypotheses are proposed to explain this discrepancy. Firstly, as for $\theta_{max-mac}$ parameter, d parameter has a nonlinear impact on the overall water flow dynamic as the sink source term is inversely proportional to the square of d (see eq. 3): the $d(z)$ profile may therefore not be directly replaced by a single value. Secondly, different values of d parameter can be compensated by different values fitted for other parameters when the model is sensitive to those parameters. This is particularly the case for parameter b that is a very sensitive parameter whose fitted values may range over several order of magnitude as already observed by Di Pietro et al. (2003) for the KDW model and Di Pietro and Lafolie (1991) for the KW model. Thirdly, the d parameter obtained from CT images may not be directly used in the sink-source term (eq. 3). Indeed, the unique numerical parameter d in eq. 3 stands for two physical parameters: a characteristic length of the mean size of aggregates (or mean distance between macropores) and a characteristic length of water diffusion from macropore walls within the inter-aggregate's spaces inside soil matrix. Eq. (3) is quite similar to sink – source terms found in MACRO (Jarvis et al., 1991) or in Gerke and van Genuchten (1993). The characteristic inter-macropore distance can be extracted from 3D CT image analysis, but the typical water diffusion length cannot be deduced from these images and should be less than the characteristic inter-macropore distance. Therefore, Gerke and van Genuchten (1993) or MACRO (Jarvis et al., 1991) introduced an empirical correcting factor in the sink-source term expression, which was not used here.

4.3 Dynamic of water exchange from macropores to soil matrix

The instantaneous profiles of water exchange rate from macropores to the soil matrix are computed and are given on Fig. 8 for the advanced model version (similar results can be found for the classical one) at10 specific times ranging from the beginning of infiltration before the breakthrough, during the pseudo-steady-state flow and up to the final phase. At the beginning of the experiment, water exchanges occur in the topsoil. Then a "water exchange

649 front" appears and propagates downwards over time . At the end of the rainfall event (t =
650 5400 s), the water exchange front is located in the deepest part of the soil column and it
651 vanishes as water drains out of the macropores.
652 For a given soil, the overall exchange rate and its evolution over time is a function of the
653 initial soil condition. For the Loamy soil at field capacity, the exchange rate is always less
654 than 1.10^{-5} $m^3.m^{-3}.s^{-1}$ and is mainly located in the upper part of the soil column: at field
655 capacity, its water retention capacity is close to zero and the horizontal gradient of the soil
656 matric potential which is the driving force of water flow from macropores to soil matrix is
657 very low (see Eq. 3). For the Loamy soil at the initial dried state (h = -3.5 m), the water
658 exchange rate can be more than 4.10^{-5} $m^3.m^{-3}.s^{-1}$ and is mainly located in the lower part of the
659 soil column. Because of this initial dried state, the water retention capacity of the soil matrix
660 and the horizontal gradient of the soil matric potential are higher and increase the exchange
661 rate.
662 For the Silty soil, there are few differences in quantity between the two initial situations,
663 probably because the so-called field capacity is not reached for this column. But there is a
664 difference in the temporality of the exchange rate: the maximum exchange is reached at
665 1000 s at field capacity and decreases before the end of the rainfall, while in the initial dried
666 state, the exchange rate reaches a maximum at 5600 s and then decreases corresponding to the
667 end of the rainfall over 200 s..
668
669 *4.4 Classical vs. advanced version of the model*
670 The classical version provides better simulations compared to the observed data: this result
671 was expected as the number of parameters to fit is greater for the classical model version (5
672 parameters to fit) than for the advanced version (3 parameters to fit). Performances of
673 advanced model are nevertheless comparable to the ones obtained by the classical model
674 except for the loamy soil at the initial matric potential of -3.5 m.
675 To synthetize our results, the different components of the water balance of the soil columns
676 during the experiments are plotted in Figure 9, showing that whatever the soil, the initial
677 water content and model version, we can check that no internal dysfunction or numerical error
678 affects the simulations as the total mass balance is always equal to zero (grey dotted line).
679 Water infiltrates and percolates through the soil mainly through the macropore network, with
680 just a small quantity of the infiltration water remaining stored in the soil.
681 However, the exchange curves differ according to the version of the model used. The classical
682 one induces little or no exchange for the two initial situations and soils. The advanced one

683 induces little exchange at field capacity: 2 mm for the Silty soil and 0.5 mm for the Loamy
684 soil, but more exchange in the initial dried state: 5 mm for the Silty soil and 10 mm for the
685 Loamy soil. We demonstrate here a different behavior between the two model versions: the
686 classical one generates little water exchange whatever the initial soil conditions, whereas the
687 advanced one generates a larger water exchange that is a function of the initial water content.
688 This highlights the importance of the exchange term and its parameterization for this type of
689 flow model with interacting porosity domains. The number of degrees of freedom is in fact
690 also an issue. Indeed, a large number of parameters will favor the smoothing of experimental
691 results by the model and even if the mass balances are good, the flux distributions do not
692 seem very coherent with the experimental situations, particularly those obtained with the
693 classical version of the model.
694

695 ## Conclusion

696 A water flow model accounting for preferential flow made by coupling the Richards' equation
697 to the Kinematic Dispersive Wave (KDW) model with a sink-source term was tested to
698 simulate water infiltration in soils. 5 physically based parameters related to the coupled model
699 (3 parameters for KWD and 2 parameters for the sink-source term) need to be fitted. We
700 showed that the two parameters of the sink-source term may be calculated from 3D images of
701 the soil structure obtained by X-ray CT scan without much loss in fit quality of the drainage
702 dynamics. This is a major benefit of our study as the number of optimized parameters is
703 therefore reduced from 5 to 3 parameters.
704 Using 3D images of the soil structure combined with the model provide an improved
705 understanding of water exchanges between the macropore network and the soil matrix. As
706 underlined by our sensitivity analysis, this process is of major importance for predicting the
707 overall drainage dynamic when the soil is drier than field capacity. We also demonstrated that
708 the profile of intermacropore spacing is a likely useful parameter to predict the overall water
709 dynamic in natural soils.
710 However, the formalism used in the model to account for water exchange from macropores to
711 soil matrix is not perfectly adapted to the information provided by the image. More research is
712 needed to improve this model and the sink–source term between macropores and soil matrix
713 with the help of high-speed functional imagery of water flow in undisturbed soil samples. A
714 short-term perspective of this work will also to characterize and quantify the evolution of
715 structural porosity over time as a function of infiltration, drying and combined cycles. As

716 other undertaken approaches, a second step will be the determination of some dynamic
717 relevant structure parameters that could be included in mass transfer models (Bagnall et al.
718 2019).

References

Bagnall, D., C.L.S. Morgan, C.C. Molling, J.L. Heilman, and G.W. Moore. 2019. Testing a water redistribution model in a cracked Vertisol at two scales. Vadose Zone J. 18:180173. doi:10.2136/vzj2018.09.0173.

Beven, K., Germann, P., 2013. Macropores and water flow in soils revisited. Water Resour. Res. 49, 3071–3092. https://doi.org/10.1002/wrcr.20156

Beven, K., Germann, P., 1982. Macropores and water flow in soils. Water Resour. Res. 18, 1311–1325. https://doi.org/10.1029/WR018i005p01311

Chen, C., Wagenet, R.J., 1992. Simulation of water and chemicals in macropore soils Part 1. Representation of the equivalent macropore influence and its effect on soilwater flow. J. Hydrol. 130, 105–126.

Clothier, B.E., Green, S.R., Deurer, M., 2008. Preferential flow and transport in soil: progress and prognosis. Eur. J. Soil Sci. 59, 2–13. https://doi.org/10.1111/j.1365-2389.2007.00991.x

Di Pietro, L., 1998. Strategies for describing preferential flow: the continuum approach and cellular-automaton fluids., in: Physical Nonequilibrium in Soils, Modeling and Application., Ann Arbor Press. pp. 437–453.

Di Pietro, L., Lafolie, F., 1991. Water flow characterization and test of a kinematic-wave model for macropore flow in a highly contrasted and irregular double-porosi medium. J. Soil Sci. 42, 551–563. https://doi.org/10.1111/j.1365-2389.1991.tb00102.x

Di Pietro, L., Ruy, S., Capowiez, Y., 2003. Predicting preferential water flow in soils by traveling-dispersive waves. J. Hydrol. 278, 64–75. https://doi.org/10.1016/S0022-1694(03)00124-0

Dirksen, C., 1998. Soil Physics Measurements [WWW Document]. URL https://www.schweizerbart.de/publications/detail/isbn/9783510653867/Dirksen_Soil_Physics_Measurements_GeoE (accessed 7.5.18).

Gerke, H.H., 2012. Macroscopic Representation of the Interface between Flow Domains in Structured Soil. Vadose Zone J. 11, 0. https://doi.org/10.2136/vzj2011.0125

Gerke, H.H., 2006. Preferential flow descriptions for structured soils. J. Plant Nutr. Soil Sci. 169, 382–400. https://doi.org/10.1002/jpln.200521955

Gerke, H.H., van Genuchten, M.T., 1993. A dual-porosity model for simulating the preferential movement of water and solutes in structured porous media. Water Resour. Res. 29, 305–319. https://doi.org/10.1029/92WR02339

Germann, P., Helbling, A., Vadilonga, T., 2007. Rivulet approach to rates of preferential infiltration. Vadose Zone J. 6, 207–220. https://doi.org/10.2136/vzj2006.0115

Germann, P.F., 1990. Preferential Flow and the Generation of Runoff: 1. Boundary Layer Flow Theory. Water Resour. Res. 26, 3055–3063. https://doi.org/10.1029/WR026i012p03055

Germann, P.F., 1985. Kinematic wave approach to infiltration and drainage into and from soil macropores. Am. Soc. Agric. Eng. 28, 745–749.

Germann, P.F., Di Pietro, L., 1996. When is porous-media flow preferential? A hydromechanical perspective. Geoderma 74, 1–21.

Germann, P.F., Di Pietro, L., Singh, V.P., 1997. Momentum of flow in soils assessed with TDR-moisture readings. Geoderma 80, 153–168. https://doi.org/10.1016/S0016-7061(97)00074-8

Gwo, J.P., Jardine, P.M., Wilson, G.V., Yeh, G.T., 1995. A multiple-pore-region concept to modeling mass transfer in subsurface media. J. Hydrol. 164, 217–237.

Hendrickx, J.M.H., Flury, M., 2001. Uniform and preferential flow mechanisms in the vadose zone., in: Conceptual Models of Flow and Transport in the Fractured Vadose Zone., National Research Council, National Academy Press, Washington, DC. pp. 149–187.

Jarvis, N., 1994. The MACRO Model (version 3.1). Swedish University of Agricultural Sciences, Department of Soil Sciences.

Jarvis, N., Boesten, J., 1998. INCORPORATING MACROPORE FLOW INTO FOCUS PEC MODELS JARVIS N., BOESTEN J. 2, HENDRIKS R. 2, KLEIN M. 3, LARSBO M., ROULIER S.

Jarvis, N., Koestel, J., Larsbo, M., 2016. Understanding Preferential Flow in the Vadose Zone: Recent Advances and Future Prospects. Vadose Zone J. 15, 0. https://doi.org/10.2136/vzj2016.09.0075

Jarvis, N.J., Jansson, P.-E., Dik, P.E., Messing, I., 1991. Modelling water and solute transport in macroporous soil. I. Model description and sensitivity analysis. J. Soil Sci. 42, 59–70. https://doi.org/10.1111/j.1365-2389.1991.tb00091.x

Katuwal, S., Norgaard, T., Moldrup, P., Lamande, M., Wildenschild, D., de Jonge, L.W., 2015. Linking air and water transport in intact soils to macropore characteristics inferred from X-ray computed tomography. Geoderma 237, 9–20. https://doi.org/10.1016/j.geoderma.2014.08.006

Mossadeghi-Björklund, M., Arvidsson, J., Keller, T., Koestel, J., Lamandé, M., Larsbo, M., Jarvis, N., 2016. Effects of subsoil compaction on hydraulic properties and preferential flow in a Swedish clay soil. Soil Tillage Res. 156, 91–98. https://doi.org/10.1016/j.still.2015.09.013

Nimmo, J.R., 2012. Preferential flow occurs in unsaturated conditions. Hydrol. Process. 26, 786–789. https://doi.org/10.1002/hyp.8380

Ruy, S., Di Pietro, L., Cabidoche, Y.M., 1999. Numerical modelling of water infiltration into the three components of porosity of a vertisol from Guadeloupe. J. Hydrol. 221, 1–19.

Saltelli, A., Tarantola, S., Chan, K.P.-S., 1999. A Quantitative Model-Independent Method for Global Sensitivity Analysis of Model Output. Technometrics 41, 39–56. https://doi.org/10.2307/1270993

Sammartino, S., Lissy, A.-S., Bogner, C., Van den Bogaert, R., Capowiez, Y., Ruy, S., Cornu, S., 2015. Identifying the Functional Macropore Network Related to Preferential Flow in Structured Soils. Vadose Zone J. 14. https://doi.org/10.2136/vzj2015.05.0070

Sammartino, S., Michel, E., Capowiez, Y., 2012. A Novel Method to Visualize and Characterize Preferential Flow in Undisturbed Soil Cores by Using Multislice Helical CT. Vadose Zone J. 11, 0. https://doi.org/10.2136/vzj2011.0100

Schaap, M.G., Leij, F.J., 2000. Improved Prediction of Unsaturated Hydraulic Conductivity with the Mualem-van Genuchten Model. Soil Sci. Soc. Am. J. 64, 843. https://doi.org/10.2136/sssaj2000.643843x

Schneider, C.A., Rasband, W.S., Eliceiri, K.W., 2012. NIH Image to ImageJ: 25 years of image analysis. Nat. Methods 9, 671–675. https://doi.org/10.1038/nmeth.2089

Tamari, S., Gaudu, J.C., Simonneau, T., 1993. Tensiometric measurement and metastable state of water under tension. Soil Sci. 156, 149–155.

Van Genuchten, M.T., 1980. A closed-form equation for predicting the hydraulic conductivity of unsaturated soils. Soil Sci. Soc. Am. J. 44, 892–898.

Vrugt, J.A., 2016. Markov chain Monte Carlo simulation using the DREAM software package: Theory, concepts, and MATLAB implementation. Environ. Model. Softw. 75, 273–316. https://doi.org/10.1016/j.envsoft.2015.08.013

Vrugt, J.A., Diks, C.G.H., Clark, M.P., 2008. Ensemble Bayesian model averaging using Markov Chain Monte Carlo sampling. Environ. Fluid Mech. 8, 579–595. https://doi.org/10.1007/s10652-008-9106-3

Wind, G.P., 1969. Capillary conductivity data estimated by a simple method.

818 **Figure legends**

819 **Fig. 1.** Scheme of the experimental device for lab infiltration experiments composed of a
820 rainfall simulator connected to a pulse pump (not shown in the scheme) and three precision
821 scales (B1, B2 and B3) connected to a computer. The volume recorded by the medical scanner
822 is surrounded by a dotted line.

823 **Fig. 2.** Flowchart illustrating the main processing steps applied to the 3D images.

824 **Fig. 3.** Temporal evolutions of the main (dotted lines) and the total (continuous line)
825 contribution indexes of KDW and sink-source term parameters for the classical version of the
826 model. The sensitivity analysis is made with 1200 cumulative drainage curves. The initial
827 water content is given as follow: "FC" for field capacity and "DS" for the dried state (matric
828 potential of -3.5 m).

829 **Fig. 4.** (a) Drainage curves for the four experiments simulated by the classical and advanced
830 versions of the model (referenced respectively as version 1 and version 2) compared to the
831 experimental data (referenced as observed data). (b) Absolute value of the difference between
832 the experiment and model versions. The initial water content is given by: "FC" for field
833 capacity and "DS" for the dried state (matric potential of –3.5 m).

834 **Fig. 5.** (a) Storage curves for the four experiments simulated by the classical and advanced
835 versions of the model compared to the experimental data. (b) Absolute value of the difference
836 between the experiment and model versions. The initial water content is given by: "FC" for
837 field capacity and "DS" for dried state (matric potential of – 3.5 m).

838 **Fig. 6.** Three-dimensional rendering of sample macroporosities at field capacity. The
839 percolating macroporosity is in red and its complementary is in blue. a) Loamy sample. b)
840 Silty sample.

841 **Fig. 7.** Z-profiles of macroporosities and mean inter-macropore distances. a) Loamy soil. b)
842 Silty soil. The initial water content is referred as "FC" for field capacity and "DS" for dried
843 state (matric potential of – 3.5 m). "P" refers to the percolant part of the macroporosity.

844 **Fig. 8.** Z-Profiles of water exchange between macropores to soil matrix for the two soil types
845 and the two initial conditions. The initial water content is referred as "FC" for field capacity
846 and "DS" for dried state (matric potential of -3.5 m).

847 **Fig. 9.** Water mass balance in macropores for the four simulated rainfall experiments with the
848 classical (left) and advanced (right) versions of the model. Cumulated rainfall input (black
849 line), mass balance between water infiltration, drainage and storage (dotted line in grey).
850 Detailed mass balances: surface water infiltration in macropores (blue), water exchanges
851 between macropores to micropores (yellow), drainage (green) and storage in macropores. The
852 initial water content is referred as "FC" for field capacity and "DS" for the dried state (matric
853 potential of –3.5 m).

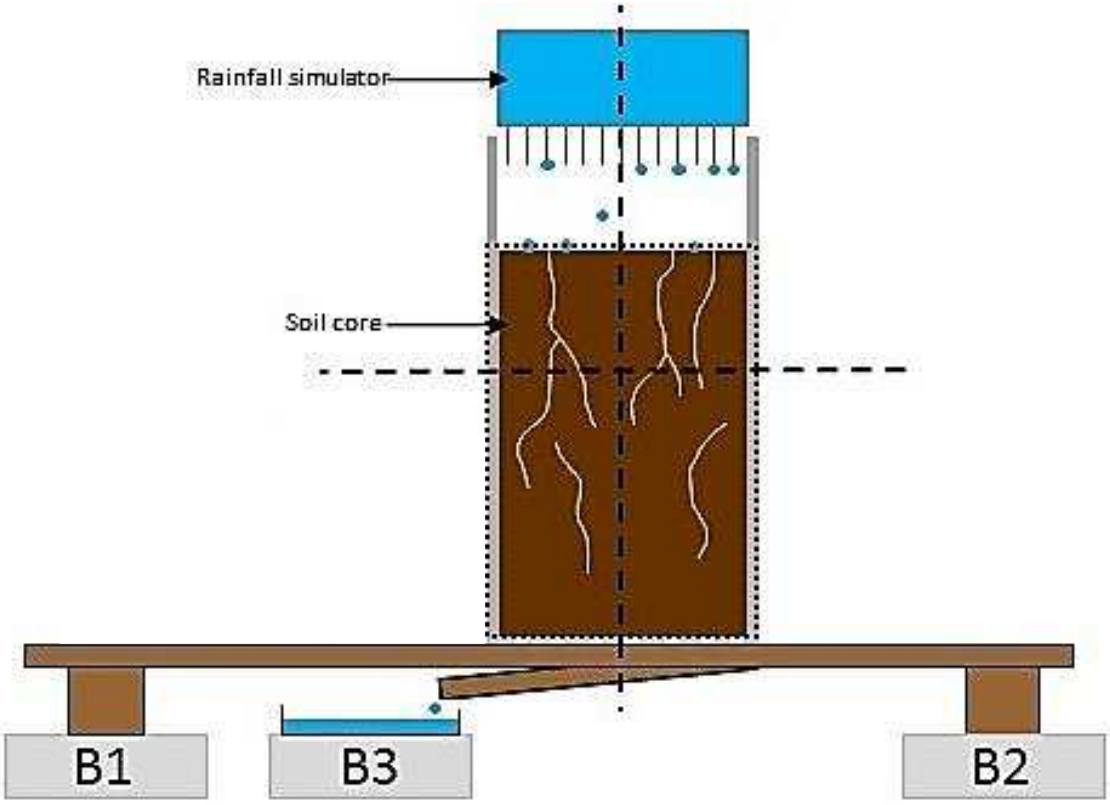
Rainfall simulator
Soil core
B1
B3
B2

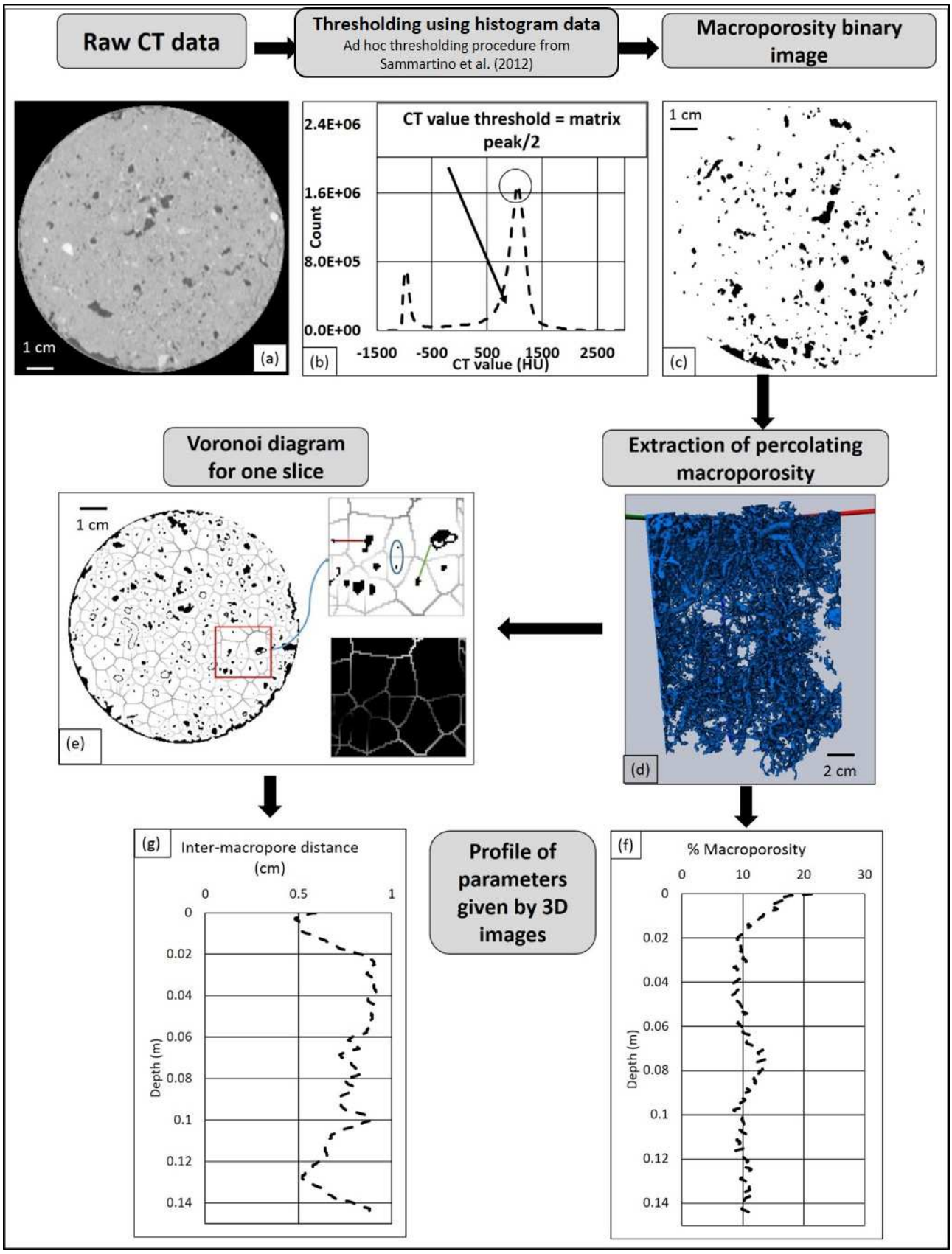
Raw CT data
Thresholding using histogram data
Ad hoc thresholding procedure from Sammartino et al. (2012)
Macroporosity binary image
1 cm
(a)
CT value threshold = matrix peak/2
2.4E+06
1.6E+06
8.0E+05
0.0E+00
Count
-1500
-500
500
1500
2500
CT value (HU)
(b)
1 cm
(c)
Extraction of percolating macroporosity
Voronoi diagram for one slice
1 cm
(e)
(d)
2 cm
(g)
Inter-macropore distance (cm)
0
0.5
1
Depth (m)
0
0.02
0.04
0.06
0.08
0.1
0.12
0.14
Profile of parameters given by 3D images
(f)
% Macroporosity
0
10
20
30
Depth (m)

(a) Loamy soil FC

$a = 3$

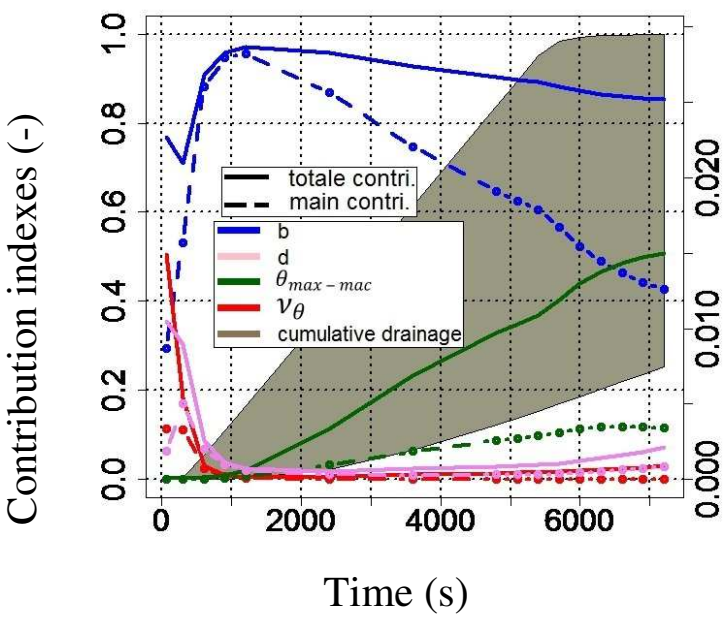

(b) Loamy soil DS

$a = 3$

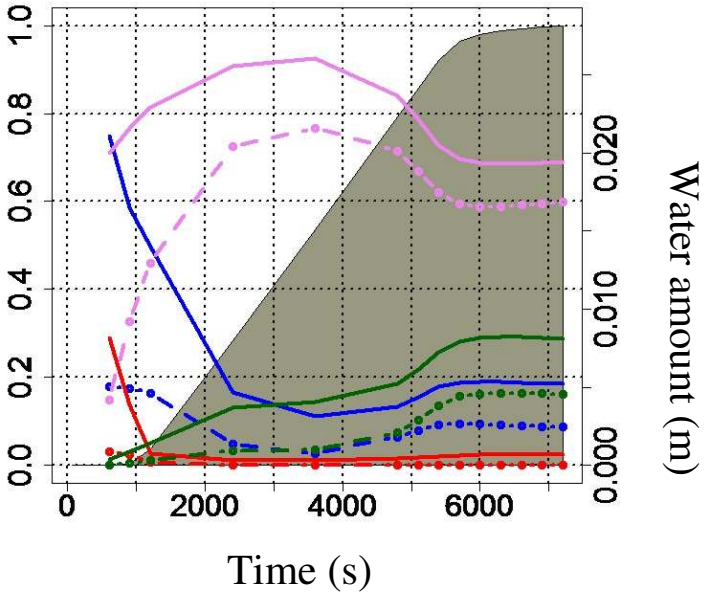

(c) Silty soil FC

$a = 5$

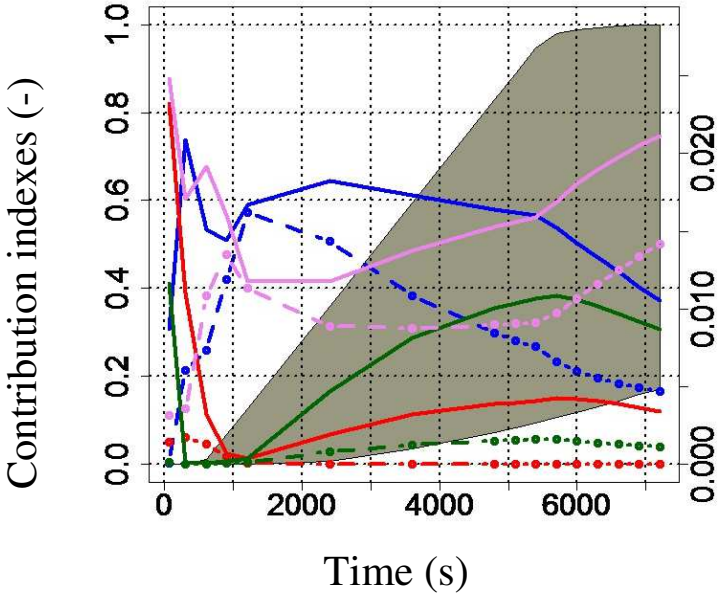

(d) Silty soil DS

$a = 5$

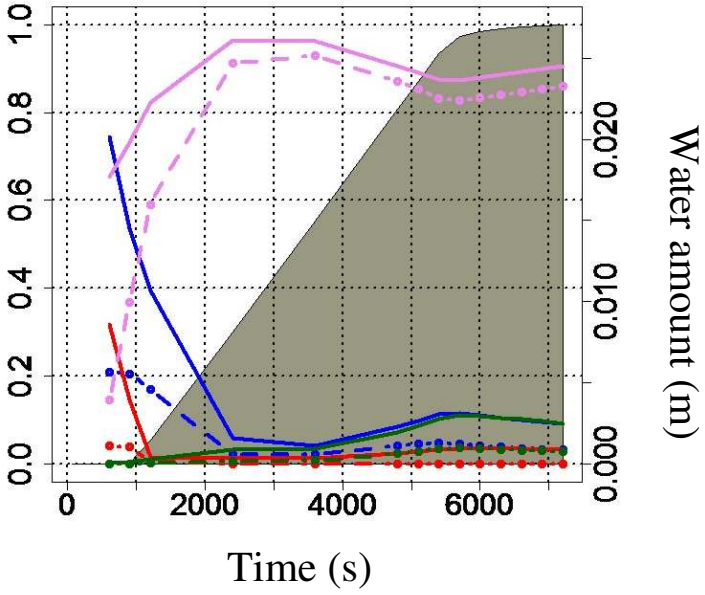

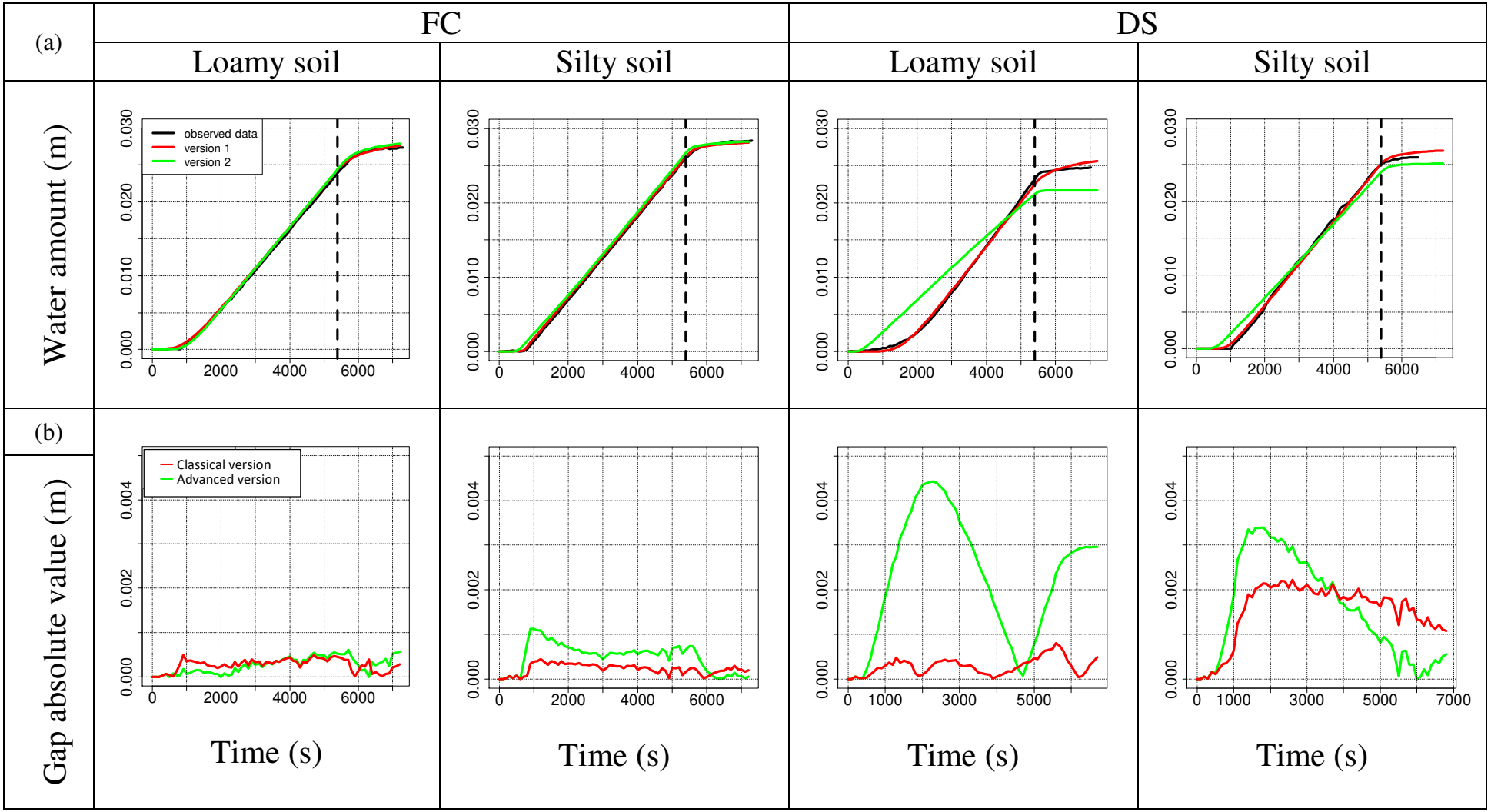
(a)
FC
DS
Loamy soil
Silty soil
Loamy soil
Silty soil
Water amount (m)
observed data
version 1
version 2
0.000
0.010
0.020
0.030
0
2000
4000
6000
(b)
Gap absolute value (m)
Classical version
Advanced version
0.000
0.002
0.004
0
1000
2000
3000
4000
5000
6000
7000
Time (s)
Time (s)
Time (s)
Time (s)

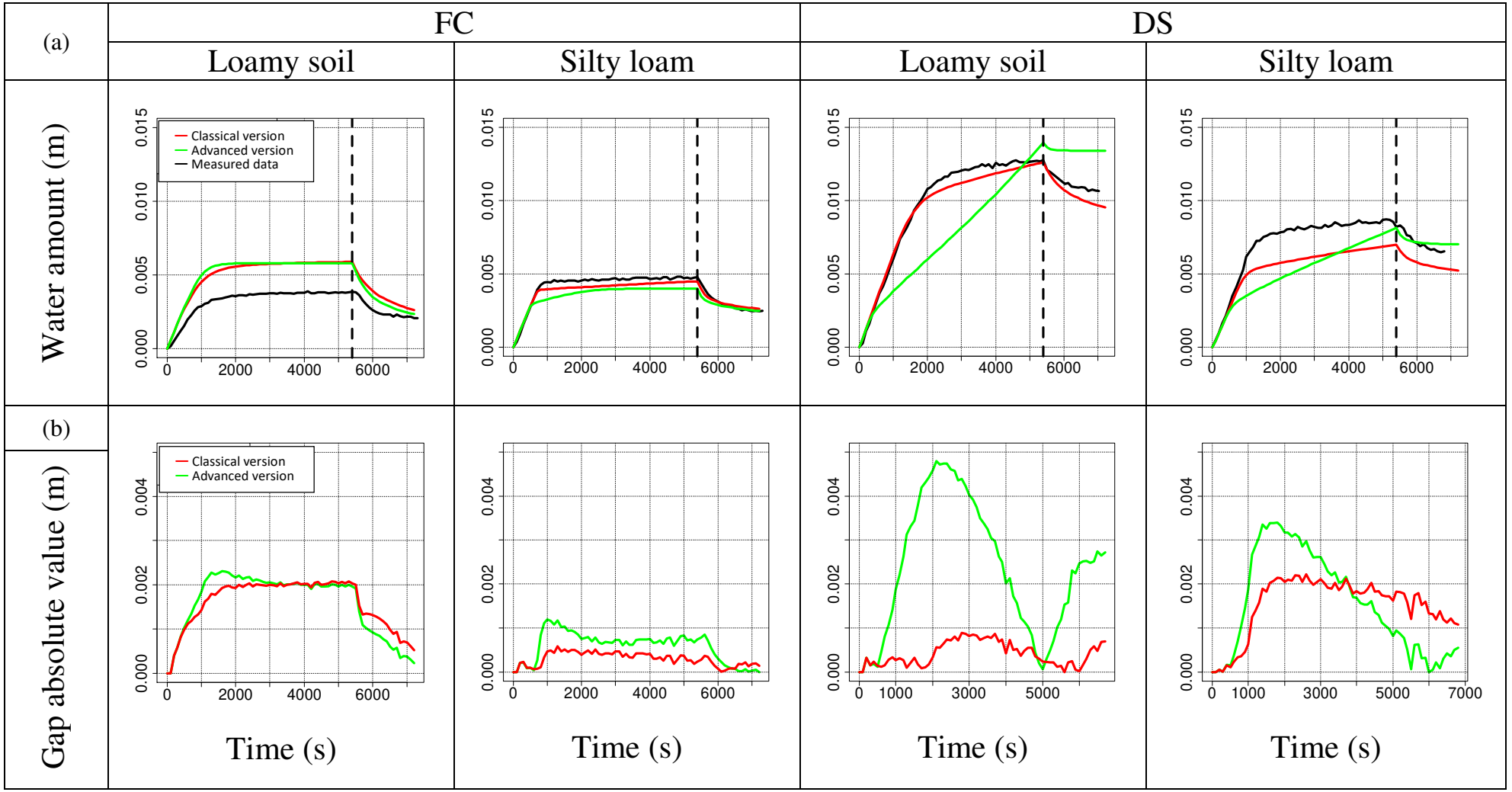
(a)
FC
DS
Loamy soil
Silty loam
Loamy soil
Silty loam
Water amount (m)
Classical version
Advanced version
Measured data
0.000
0.005
0.010
0.015
0
2000
4000
6000
(b)
Gap absolute value (m)
Classical version
Advanced version
0.000
0.002
0.004
0
1000
2000
3000
4000
5000
6000
7000
Time (s)
Time (s)
Time (s)
Time (s)

a)

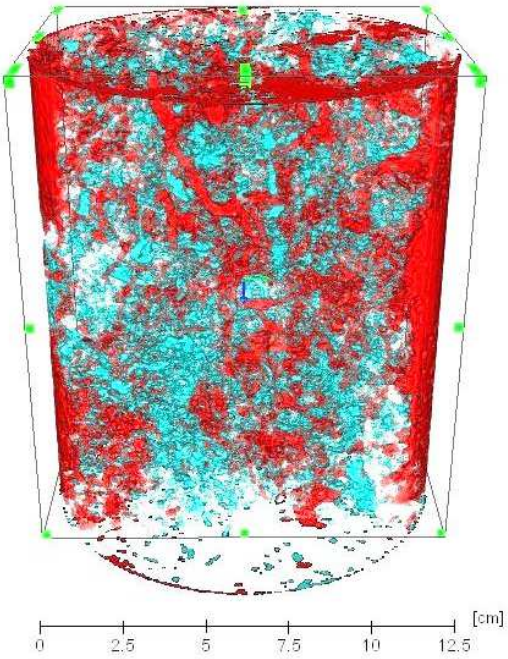

b)

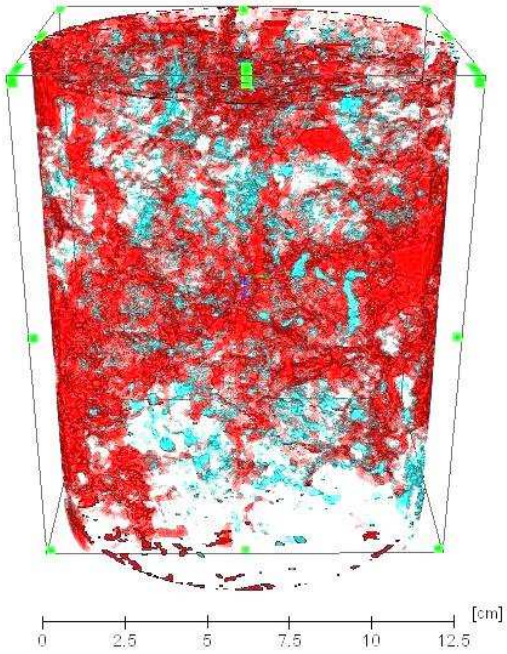

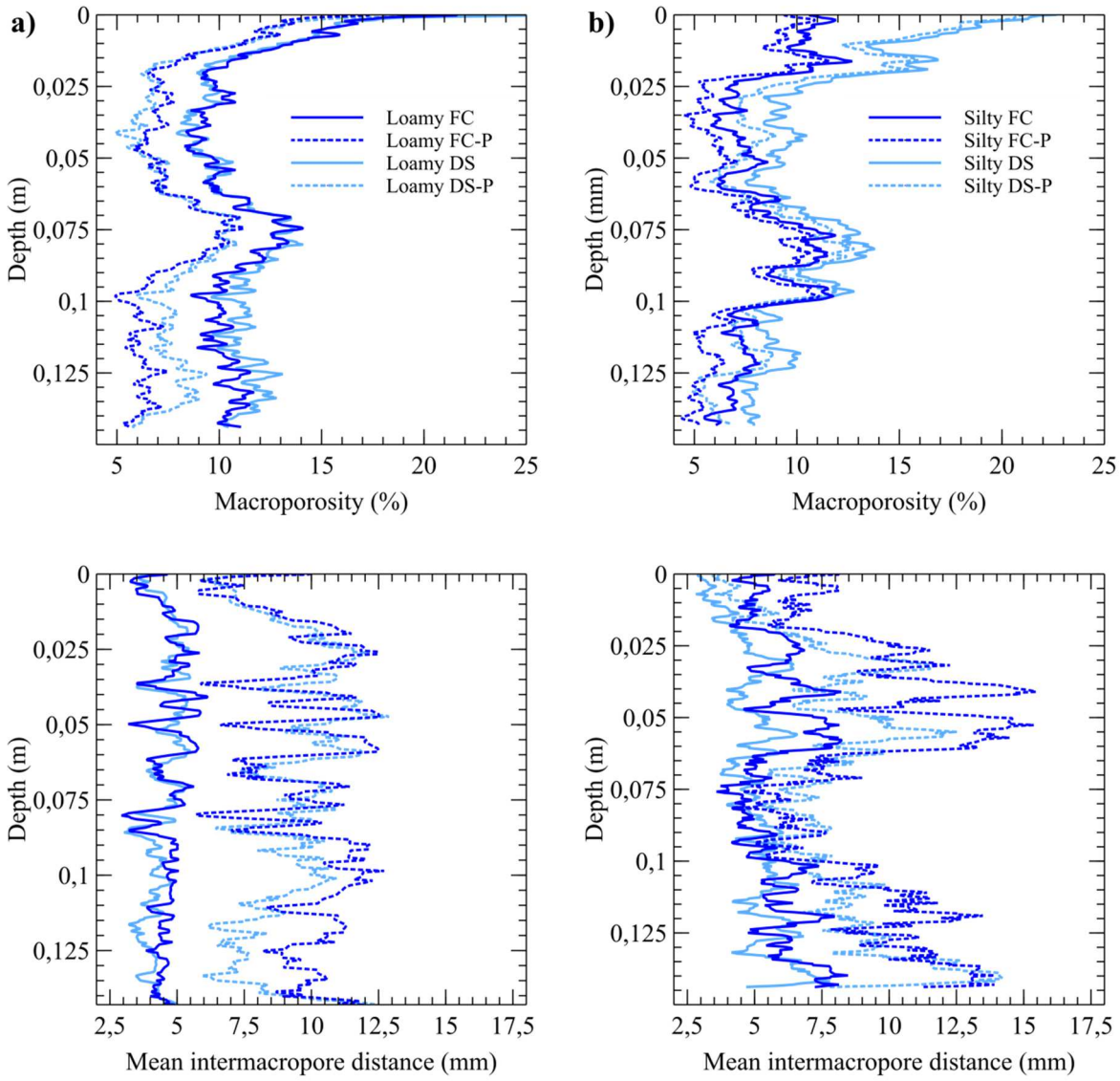
a)
b)
Depth (m)
Depth (mm)
Loamy FC
Loamy FC-P
Loamy DS
Loamy DS-P
Silty FC
Silty FC-P
Silty DS
Silty DS-P
Macroporosity (%)
Mean intermacropore distance (mm)
0
0,025
0,05
0,075
0,1
0,125
5
10
15
20
25
2,5
7,5
12,5
17,5

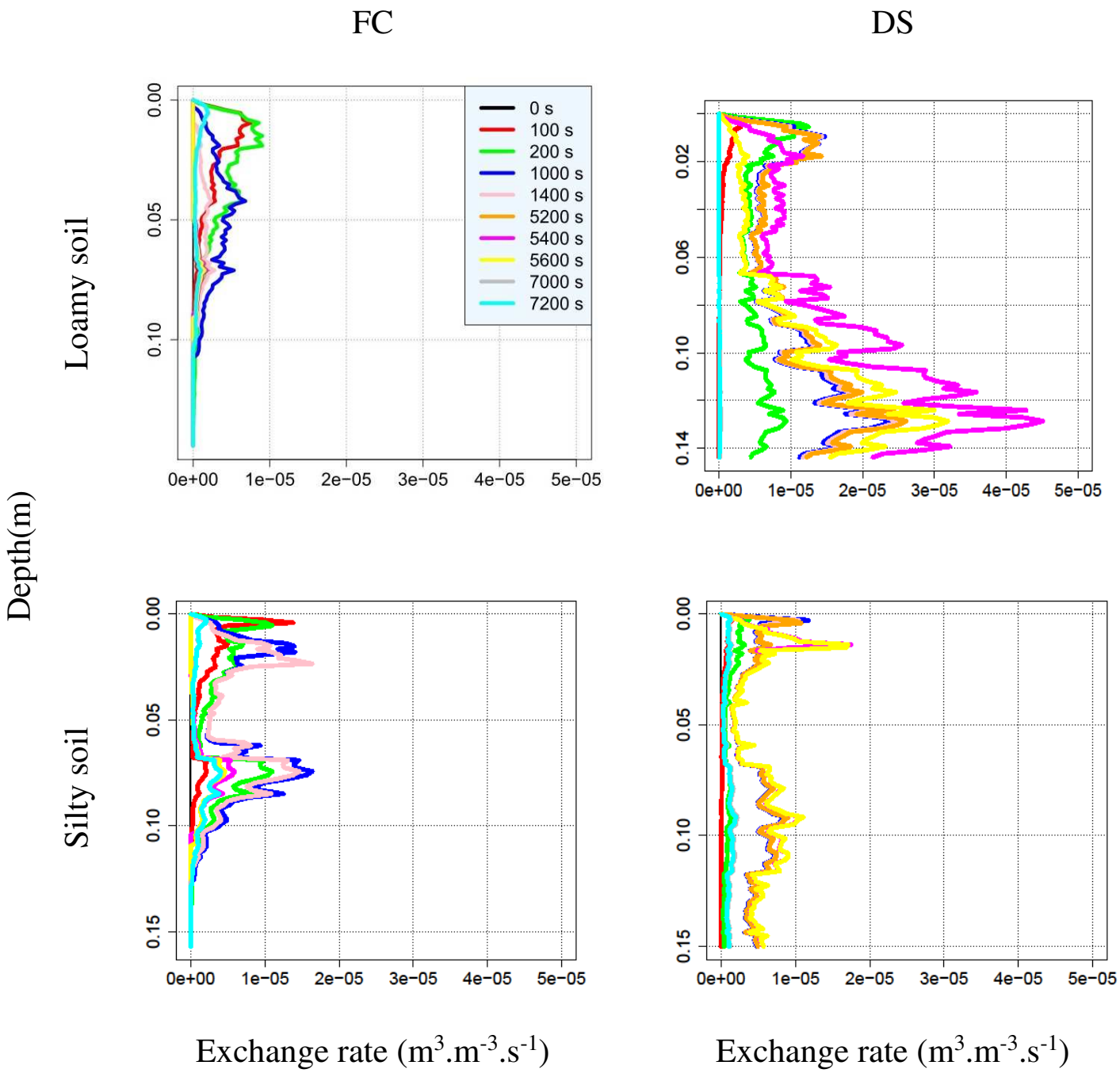
FC
DS
Loamy soil
Silty soil
Depth(m)
0 s
100 s
200 s
1000 s
1400 s
5200 s
5400 s
5600 s
7000 s
7200 s
0.00
0.05
0.10
0.15
0.02
0.06
0.14
0e+00
1e-05
2e-05
3e-05
4e-05
5e-05
Exchange rate (m3.m-3.s-1)
Exchange rate (m3.m-3.s-1)

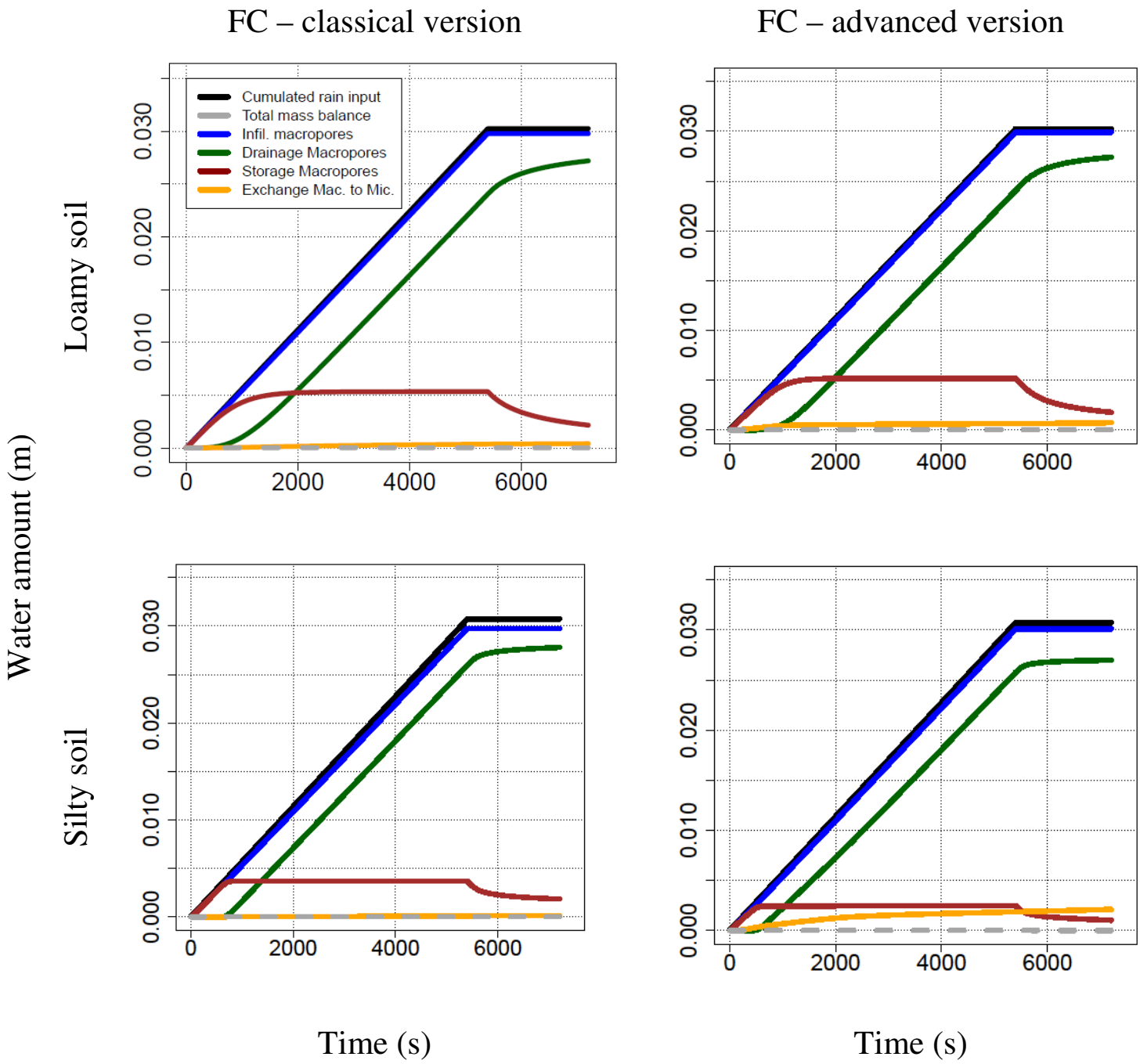
FC – classical version
FC – advanced version
Loamy soil
Silty soil
Water amount (m)
Time (s)
Time (s)
Cumulated rain input
Total mass balance
Infil. macropores
Drainage Macropores
Storage Macropores
Exchange Mac. to Mic.
0.000
0.010
0.020
0.030
0
2000
4000
6000

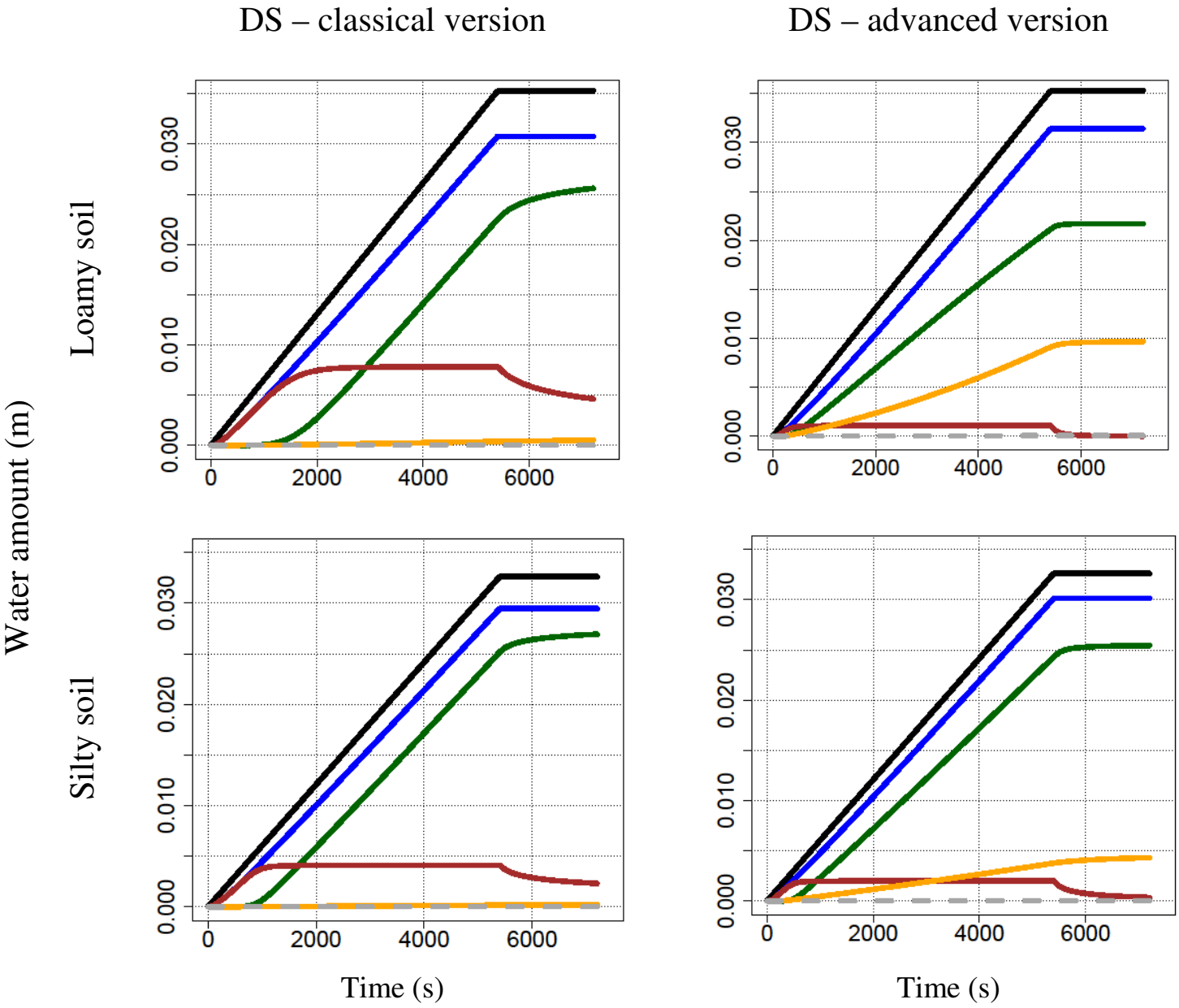
DS – classical version
DS – advanced version
Loamy soil
Silty soil
Water amount (m)
Time (s)
Time (s)
0.000
0.010
0.020
0.030
0
2000
4000
6000

Table 1. Soil textural characteristics and sample dimensions.

Soil core dimensions / Soil texture	Loamy sample	Silty sample
Core height (m)	0.138	0.157
Core diameter (m)	0.125	0.125
Sand fraction (%)	37.7	1.50
Silt fraction (%)	48.7	53.9
Clay fraction (%)	13.6	44.6

Table 2. Parameters of hydrodynamic curves for soils (* fixed values, ** adjusted).

Parameters			Significance – unity	**Silty soil (0-7 cm) Wind 1**	**Silty soil (7-14 cm) Wind 2**	**Loamy soil (0-7 cm) Wind 1**	**Loamy soil (7-14 cm) Wind 2**
Adjusted hydraulic parameters (microporosity domain)	$\boldsymbol{h(\theta)}$ **	θ_{sat}	Saturated water content ($m^3.m^{-3}$)	0.47	0.42	0.37	0.38
		θ_{res}	Residual water content ($m^3.m^{-3}$) *	0	0	0	0
		α	Structural parameter (m^{-1})	4.5438	4.4734	4.2898	2.0155
		n	Dimensionless parameter (-)	1.0987	1.0778	1.1776	1.2562
	$\boldsymbol{K(\theta)}$ **	θ_{sat}	Saturated water content ($m^3.m^{-3}$)	0.46	0.42	0.43	0.47
		θ_{res}	Residual water content ($m^3.m^{-3}$)	0	0	0	0
		$K_{sat-mic}$	Saturated fitted hydraulic conductivity ($m.s^{-1}$)	$4.55.10^{-08}$	$1.82.10^{-7}$	$6.71.10^{-07}$	$2.50.10^{-06}$
		n	Dimensionless parameter (-)	1.2755	1.1815	1.4285	1.4268
		$tortuosity$	Tortuosity factor (-) *	0.5	0.5	0.5	0.5
Measured hydraulic parameters on Wind samples (undisturbed samples: microporosity and macroporosity domains)	**$\boldsymbol{\theta_{init-meas}}$ measured at the beginning of the experiment ($m^3\ m^{-3}$)**			0.45	0.42	0.37	0.38
	Porosity ($m^3\ m^{-3}$)			0.45	0.43	0.48	0.47
	$K_{sat-meas}$ ($m.s^{-1}$)			$3.16.10^{-04}$	$6.58.10^{-04}$	$3.38.10^{-04}$	$3.54.10^{-05}$
	Bulk density ($g.cm^{-3}$)			1.48	1.52	1.40	1.41

Table 3. KDW and sink – source term parameters, and range of variation for the DREAM algorithm.

Range of values	**Macropores shape parameter**	**Kinematic coefficient**	**Diffusion coefficient**	**Inter – macropore distance**	**Maximal water content in macroporosity**
	$a\ (-)$	$b\ (m.s^{-1})$	$\nu_\theta\ (m)$	$d\ (m)$	$\theta_{max-mac}(m^3.m^{-3})$
Classical version	$[\,1\,;\,6]$	$[\frac{b_{th}}{5}; b_{th} \times 5]$	$[\,5.10^{-3}; 10^{-1}]$	$[10^{-4}; 10^{-1}]$	$\left[\frac{\theta_{max-mac-meas}}{2}; \theta_{max-mac-meas} \times 2\right]$
Advanced version	$[\,1\,;\,6]$	$[\frac{b_{th}}{5}; b_{th} \times 5]$	$[\,5.10^{-3}; 10^{-1}]$	Calculated from CT profile	Calculated from CT profile

Table 4. Parameters of KDW and of the sink-source term, estimated for the classical and advanced versions of the model. "FC" refers to the field capacity state and "DS" refers to the dried state at h = -3.5 m. * Values calculated from CT images.

Parameters	**FC**				**DS**			
	Loamy soil		Silty soil		Loamy soil		Silty soil	
	Classical	Advanced	Classical	Advanced	Classical	Advanced	Classical	Advanced
$\boldsymbol{a}\ (-)$	2.5	2.5	5.0	5.3	4.4	1.7	5.4	2.8
$\boldsymbol{b}\ (\mathbf{m}.\mathbf{s}^{-1})$	$2.3.10^{-2}$	$2.3.10^{-2}$	$9.1.10^{+2}$	$2.1.10^{+4}$	2.2	$3.2.10^{-2}$	$1.7.10^{+3}$	1.3
$\boldsymbol{v_\theta}\ (\boldsymbol{m})$	$1.1.10^{-4}$	$1.1.10^{-5}$	$1.1.10^{-5}$	$1.1.10^{-5}$	$1.2.10^{-3}$	$2.8.10^{-5}$	$8.7.10^{-4}$	$3.8.10^{-5}$
$\boldsymbol{d}\ (\boldsymbol{m})$	0.027	0.0083	0.095	0.0087	0.066	0.0074	0.044	0.0075
$\boldsymbol{\theta_{max-mac}}\ (-)$	0.058	0.056*	0.074	0.054*	0.072	0.060*	0.066	0.067*

Table 5. Entire and percolating macroporosity, mean inter-macropore distance for the two initial water contents and the two studied soils, and the percolating fraction of the entire macroporosity. "FC" refers to the field capacity state and "DS" refers to the dried state at h = -3.5 m.

Macroporosity type	**Entire**				**Percolating**			
Soil type & initial water content	Loamy FC	Loamy DS	Silty FC	Silty DS	Loamy FC	Loamy DS	Silty FC	Silty DS
Macroporosity (%)	10.9	11.2	8.4	10.7	7.7	8.2	7.2	9.3
Mean inter–macropore distance (mm)	4.6	4.4	5.8	5.0	9.8	9.2	9.3	7.8
Fraction of percolating macroporosity (%)	70.6	72.6	85.5	87.4	100			